

NEUTRON PHASE CONTRAST TOMOGRAPHY ON ISOTOPE MIXTURES

*M. Zawisky¹, U. Bonse², Z. Hradil³, J. Rehacek³

¹ Atominstitute of the Austrian Universities, Vienna, Austria;

² University of Dortmund, Dortmund, Germany;

³ Palacky University, Olomouc, Czech Republic;

*Corresponding author: M. Zawisky

Stadionallee 2, A-1020 Vienna

zawisky@ati.ac.at

Fax: +431 58801 14199

Tel: +431 58801 14170

PACS: 03.75.Dg, 42.30.Wb, 87.59.Fm

Abstract

Perfect crystal neutron interferometry is an extreme sensitive instrument for the detection of phase shifts induced in materials or magnetic fields. The utilization of neutron beams and phase signals in tomography permits the investigation of weakly absorbing substances and isotope mixtures. The tomographic reconstruction of phase projections is similar to that of intensity projections in conventional transmission tomography, but due to the larger fluctuation of count numbers and phases, an optimized maximum-likelihood algorithm has to be engaged. We present the analysis of isotope mixtures, which are nearly transparent to thermal neutrons, and found a sensitivity of about 1% in the detection of isotopic density differences.

1. Introduction

PCT (*Phase Contrast Tomography*) was first invented in x-ray tomography [1,2], and has then successfully been transferred to neutron interferometry [3]. The perfect crystal interferometer is an extreme sensitive device for the detection of scattering effects in the sample [4]. The coherent forward scattering in materials or magnetic fields yields detectable phase differences between the two interfering beams, the object beam through the sample, and the reference beam (fig. 1). While x-ray PCT is sensitive to the electron density and the atomic number Z , the neutron (nPCT) technique depends solely on nuclear and magnetic interaction. Therefore, x-ray and neutron PCT are complementary techniques, always sensing different material features. Moreover, the nPCT sensitivity is three orders of magnitude higher than that of conventional CT for most isotope mixtures. Thus, the sensitive detection of isotopic density variations, and of residues in metal alloys are promising future nPCT

applications. In the following section we introduce the principles of phase imaging and summarize the experimental requirements for nPCT. Then nPCT measurements on sulphur and H₂O/D₂O mixtures of an isotope gauge are presented. The low count numbers in interferometric imaging always require an optimized data treatment, the maximum-likelihood reconstruction technique serves for that purpose, it will be introduced in the last section.

Principles and experimental requirements for interferometric imaging

The principle of interferometric imaging is sketched in fig. 1. The entrance beam, monochromatic neutrons of wavelength $\lambda \cong 0.192$ nm, is coherently split into the reference beam and the object beam at the first crystal lamella. Then the object beam passes the sample and experiences phase shifts, which cause detectable phase differences between the object and reference rays. Finally, the phase shifts Φ through the sample create, after superposition with the reference beam, an interference image in the digital neutron camera (fig. 2). The interference pattern is additionally modulated by an auxiliary phase shifter, which generates a series of controlled phase differences Δ_j between object and reference beams. The unknown phases Φ_{xz} are then inferred from the phase-modulated count numbers:

$$n_{xz,j} = \bar{n}_{xz} \left(1 + V_{xz} \cos(\Delta_j + \Phi_{xz}) \right) \quad (1)$$

\bar{n}_{xz} is the mean count number and V_{xz} the visibility of interference fringes. The visibility depends on the quality of the interferometer setup, but it is also affected by dephasing in the specimen. Low visibilities indicate a large gradient of scattering densities $\Delta(N_i b_{ci})$. Although dephasing reduces the visibility and the phase sensitivity, it contains useful information about micro-inhomogeneities below the pixel resolution.

The most important quantity in interferometric imaging is the phase shift in the sample (fig. 2):

$$\Phi_{xz} = -\lambda \int_{\text{ray}} \sum_i (N_{xz} b_{ci})_i ds \quad (2)$$

The accumulated phase shift along a pencil beam depends on the wavelength λ , the nuclear densities N_i of the different isotopes i , and the coherent scattering length b_{ci} , which is accurately known for most isotopes [5]. The phase shift is negative for repulsive potentials, but there exist some isotopes with negative b_c , characterizing weak attractive interactions. The enhanced sensitivity of nPCT can be expressed by a gain factor $(\lambda V b_c / \sigma)$, where σ denotes the total microscopic cross section [5]. It turns out that the sensitivity in detecting small density variations ΔN_i is three orders of magnitude higher than in conventional

transmission tomography for most isotopes. But the achievable phase resolution is limited by the statistical phase uncertainty [6]:

$$\Delta\Phi_{xz} \cong \frac{\sqrt{2}}{\sqrt{n_{total,xz}} V_{xz}} \quad (3)$$

The phase uncertainty depends on the total count number $n_{total,xz} = \sum_j n_{xz,j}$, and the visibilities ($0 < V_{xz} < 1$). Under present experimental conditions ($n_{total,xz} \approx 30\text{-}800$ n, $V_{xz} \approx 0.5$) the phase resolution can reach 5° , which yields a sensitivity of $\Delta(Nb_c)/(Nb_c) \approx 10^{-2}$. Large variations of scattering lengths, e.g., $\Delta b_c = 20.82$ fm between light and heavy water, enhance the sensitivity for ΔN .

Our choice of three reference phases, $\Delta_j = 0^\circ, 120^\circ, 240^\circ$, permits the additional analysis of small angle scattering and absorption, because n_{total} is then insensitive to phase shifts. Thus, different interactions can simultaneously be analyzed with the same beams. Figures 1b,c show two sample arrangements where the effect of small angle scattering can be well distinguished from absorption. The utilization of refraction effects is known as *diffraction enhanced imaging* in small angle scattering [7, 8].

In order to achieve maximal spatial resolution an optimized thin-plate interferometer is employed, with a thickness of only 0.56 mm of the analyzer plate (fig. 3a). The interferometer crystal was cut in the focusing geometry to help minimizing phase smearing in the analyzer plate [9]. Figure 3b shows the interferometer in an aluminium cover for thermal shielding. The interferometer was mounted hanging upside down for facilitating the sample positioning and rotation (fig. 3c). The spatial resolution is mainly limited by the beam divergence, which is 0.5° at our nPCT setup S18-ILL (Institute Laue-Langevin, Grenoble), and the detector-to-sample distance. Further image blur is caused by small angle scattering. This is the reason why we actually prefer the arrangement of fig. 1b over that of fig. 1c. In fig. 1b small angle scattering is removed since it is no longer Bragg reflected in the analyzer plate. In the present experiment we achieve a resolution of $50 \mu\text{m}$ in horizontal and vertical direction, which corresponds to the pixel size of the neutron camera. The position-sensitive detector uses a neutron-to-visible-light converter coupled to a CCD camera. It has 512×512 pixels with a nominal size of $50 \times 50 \mu\text{m}^2$ [10]. A further increase in spatial resolution would require a better beam collimation, higher intensities, and a high-resolving detector.

The sample sizes are limited by the geometry of the prototype interferometer to about $10 \times 25 \text{ mm}^2$. The utilizable thickness depends on the absorption and dephasing in the

specimen. In the present beam geometry (fig. 1b) the maximum sample thickness is restricted to 10 mm.

Phase analysis on isotope mixtures

All phase tomographic investigations have been performed at the Institute Laue-Langevin, instrument S18, where monochromatic neutrons with high intensity (~ 2000 n/s \cdot cm 2) are available. The specimen was primarily designed as gauge for exploiting the nPCT resolution, and for developing an optimized maximum-likelihood routine. To demonstrate the superiority of nPCT compared with conventional transmission tomography we have chosen weakly absorbing substances, like sulphur isotopes and mixtures of light and heavy water. The specimen consists of different sulphur isotope mixtures, pressed in a central bore hole as sketched in fig. 4a. The sample holder consists of an aluminium rod which is inserted in an Al-block of same composition (fig. 3c). The Al-block serves as ‘parallel-sided sample cell’ to avoid large phase differences simply caused by the cylindrical sample shape. The sulphur isotopes are invisible in the transmission image because of their negligible absorption cross sections (fig. 4c). The unprocessed images shown in fig. 4b are created by interference between the object and the reference beams at three phase shifter positions. The three images in the top row of fig. 4b are mainly phase contrast images because small angle scattering is removed with the sample in beam I. Only in the ($S_{\text{element}} + \text{Al}_2\text{O}_3$) region strong small angle scattering is revealed as strong attenuation in position I. It corresponds to the bright scattering offset seen in this region with the sample in beam II. This is an example how different scattering effects become distinguishable in perfect crystal interferometry.

At the top region of the rotatable sample holder two additional bore holes have been filled with mixtures of light and heavy water. The difference in D $_2$ O mass fraction is 4×10^{-3} but the phase sensitivity was still sufficient to resolve such small variations. To quantify phase sensitivity it is necessary to evaluate the scattering densities of the different isotope mixtures. Table 1 compares calculated and measured phase differences between some selected mixtures.

A sensitivity of detecting nuclear density variations $\Delta N/N$ at a 1% level has been confirmed in the phase analysis, with a spatial resolution of 50 μm in the phase projections.

Maximum-likelihood reconstruction

For the tomographic analysis we used 30 phase projections, *i.e.*, 30×3 interference images. Compared to the conventional tomography based on absorption the full

reconstruction of the non-absorbing isotope gauge based on phase shifts is considerably more involved due to smaller counted numbers and large total phase shifts up to $\sim 1000^\circ$ induced by the isotopes. The resulting phase jumps are difficult to correct because of the large statistical noise and the limited detector resolution. For that reason, it is advantageous to replace the standard filtered-backprojection algorithm by the more sophisticated maximum-likelihood (ML) method. The log-likelihood of the given distribution of the scattering density reads,

$$\log L = \sum_{p,j} n_{jp} \log \left[\bar{n}_p \left(1 + V_p \cos(\Delta_{jp} + \Phi_p) \right) \right] - n_{sum} M \rightarrow \max \quad (4)$$

where \bar{n}_p , V_p , and Φ_p are mean count numbers, visibility and total accumulated phase corresponding to p th projection, respectively, Δ_{jp} are the auxiliary phase shifts at one of M phase shifter positions, n_{jp} are registered counts, and n_{sum} is the sum over all projections \bar{n}_p . For the purpose of reconstruction we represent the total phase by a discrete sum $\Phi_p = \sum_k c_{pk} (Nb_c)_k$, where the coefficients c_{pk} quantify the pathlength of p th projection in k th cell (fig. 2). We assumed that the statistics of the detected counts was Poissonian. A special care has to be devoted to the reference phase measurement: Since an interferometer itself shows a non-uniform phase distribution, it introduces an extra phase that has to be measured separately. Two possibilities arise. Either the reference phase is determined separately and subtracted from the total phase Φ_p prior to reconstruction, or it is included into the model and reconstructed together with the scattering density distribution. In our analysis, the former, simpler method was adopted. Although this approach is not optimal [11], it is justified provided the reference phase measurement is much more accurate (due to higher intensities and visibilities) than the phase measurement with the sample; this condition was met in our experiment.

The likelihood (4) can be maximized by an iterative procedure of the expectation-maximization type. A nice feature of ML approach is that together with phases, the visibilities corresponding to individual projections are estimated too. Since the likelihood is a weighted sum of these individual contributions, the data leading to higher visibilities have larger influence on the result. This means that unlike the standard filtered-backprojection, our ML procedure “trusts” the data with larger phase sensitivity more than data containing little or no phase information. This method is capable of handling very noisy data and, to a certain extent also 2π phase jumps. For the reconstruction, we chose a cut through the upper part of the cylinder, where sample’s geometry is not trivial, despite both intensity and visibility drop

almost down to zero in this region. This makes the experimental data a challenge for any reconstruction method. Our results are summarized in figs. 5,6. As a first trial, we averaged data over 10 adjacent slices to increase the signal-to-noise ratio. Note that no binning in the transversal direction was done, thus, we could exploit the full 50 μm resolution of the detector. As can be seen in fig. 5c, the water filled cylinders as well as the central cylinder filled with a mixture of sulphur element and aluminium oxide are revealed in the reconstructed image. Given the extreme experimental conditions (small intensities, bad visibility, only 30 measured projections), and given that data without any prior filtering were used, the result is surprisingly good. Panels 5a and 5b depict two particular line profiles of the scattering density. Profile 5a suggests that both water mixtures have only slight differences in the scattering cross sections, which is consistent with the analysis of the previous section. As a second step, we applied the same routine to a single slice of 50 μm thickness, see fig. 5d. Though noise is significantly increased, it is still possible to distinguish the geometry of the isotope distribution. We would like to emphasize that in this case, typical counts were around 30 particles detected per pixel. Yet the ML reconstruction was able to give a meaningful result.

ML phase contrast reconstructions of different regions of the isotope sample are compared in fig. 6. Again, the geometry of the internal isotope distribution is plainly seen in all the reconstructed images. Notice that the noise seen in the images decreases from the left to the right. This is due to the illuminating conditions - during the experiment, the mean counts per pixel registered in the central region of the sample were several times higher than on its top and bottom edges, see fig. 4b.

Conclusions

We applied the recently developed neutron phase contrast tomography to isotope mixtures and could achieve a high sensitivity of about 1% in the analysis of nuclear density variations. A spatial resolution of 50 μm in the phase contrast images has been confirmed. The nPCT performance is mainly limited by the availability of intense, well-collimated, and monochromatic neutrons. But the new developed maximum-likelihood algorithm can partly compensate the statistical fluctuations. As future nPCT applications we consider the sensitive 3D analysis of weakly absorbing substances and isotope distributions, residues and corrosion in metals, and the investigation of magnetic domains in bulk materials [12].

Acknowledgement

This work was financially supported by the EURATOM-ÖAW, UT4-Underlying Technology project, and grant No. LN00A015 of the Czech Ministry of Education. The hospitality of the Institute Laue-Langevin is gratefully acknowledged.

References

- [1] Momose A., Nucl. Instr. and Meth. A, 352 (1995) 622.
- [2] Beckmann F., Bonse U., Busch F., Günnewig O., J. Comput. Assist. Tomogr., 21(4) (1997) 539.
- [3] Dubus F., Bonse U., Zawisky M., Baron M., Loidl R., IEEE Transactions of Nuclear Science, in print.
- [4] Rauch H., Werner S.A., *Neutron Interferometry*, Oxford University Press (2000).
- [5] Sears V.F., Neutron News, Vol. 3, No. 3 (1992) 26.
- [6] Rauch H., Summhammer J., Zawisky M., Jericha E., Phys. Rev. A, 42 (1990) 3726.
- [7] Treimer W., Feye-Treimer U., Herzig C., Physica B, 241-243 (1998) 1197.
- [8] Hainbuchner M., Villa M., Kroupa G., Bruckner G., Baron M., Amenitsch H., Seidl E., Rauch H., J. Appl. Cryst., 33 (2000) 851.
- [9] Becker P., Bonse U., Dettmer A., Dubus F., Zawisky M., Cryst. Res. Technol., 36 (2001) 589.
- [10] Dubus F., Bonse U., Biermann Th., Baron M., Beckmann F., Zawisky M., Proc. of SPIE, 4503 (2002) 359.
- [11] Rehacek J., Hradil Z., Zawisky M., in preparation.
- [12] Badurek G., Buchelt R.J., Leeb H., Szezywerth R., Physica B, 335 (2003) 114.

Table 1 Maximal phase differences between selected isotope mixtures

Isotope mixtures	Scattering density (Nb_c)	Diameter of the bore hole (d)	Expected phase difference	Measured phase difference
0.956 H ₂ O + 0.044 D ₂ O 0.960 H ₂ O + 0.040 D ₂ O	$-2.55 \times 10^9 \text{ cm}^{-2}$ $-2.82 \times 10^9 \text{ cm}^{-2}$	1.5 mm 1.5 mm	45° (max)	$36^\circ \pm 9^\circ$
0.95 ³³ S + 0.05 ³⁴ S 0.90 ³³ S + 0.10 ³⁴ S	$1.725 \times 10^{10} \text{ cm}^{-2}$ $1.703 \times 10^{10} \text{ cm}^{-2}$	2 mm 2 mm	48° (max)	$45^\circ \pm 8^\circ$
0.993 ³³ S Al-block	$1.745 \times 10^{10} \text{ cm}^{-2}$ $2.147 \times 10^{10} \text{ cm}^{-2}$	1 mm 1 mm	442° (max)	$407^\circ \pm 21^\circ$

Figure captions

Fig. 1

- a) The nPCT principle; the isotope mixtures inside the sample holder are viewed under different projection angles θ in the tomographic measurement.
- b) Present arrangement; if the specimen is placed in beam I, then small angle scattered neutrons are removed because they cannot fulfill the Bragg condition in the analyzer plate.
- c) Sample in beam II, here small angle scattering contributes to the output intensity.

Fig. 2 The accumulated phase shifts in the sample have to be discretized in order to apply the maximum-likelihood algorithm.

Fig. 3

- a) The first prototype of the focusing thin-plate interferometer.
- b) Aluminium cover for thermal shielding.
- c) Present nPCT arrangement; the interferometer is mounted upside down in order to facilitate the sample positioning; the sample holder (Al-rod, $\varnothing = 7$ mm) was inserted in an Al-block ($d = 8$ mm) for phase compensation.

Fig. 4 Isotope gauge for the derivation of the present nPCT resolution.

- a) Different mixtures of sulphur isotopes, pressed in the central bore hole; two smaller holes are filled with H_2O/D_2O mixtures.
- b) Phase-sensitive images taken at three reference phases Δ_j ; with the sample in beam I the small angle scattering artifacts are removed.
- c) Conventional transmission image of the gauge.

Fig. 5 ML phase contrast tomography of a cut through the upper part of the isotope gauge. Reconstructed scattering densities (in arbitrary units) are shown,

- a) along a line connecting the water cylinders with $(\Delta N b_c) / N b_c \sim 10\%$ between the two water mixtures, as expected from table 2;
- b) along a line through the central sulphur mixture, where the scattering density is considerably lower.
- c) 2D visualization of the whole slice after averaging over 10 slices.
- d) Reconstruction of a single slice of $50 \mu\text{m}$ thickness in the same region; the reconstructed

area covers 160×160 detector pixels or $8 \times 8 \text{ mm}^2$.

Fig. 6 ML reconstruction of three different regions of the isotope sample. The cuts are through (a) the uppermost region (water cylinders + central aluminium oxide/elementary sulphur cylinder); (b) $0.95 \text{ }^{33}\text{S} + 0.05 \text{ }^{34}\text{S}$ region, and (c) ^{33}S region. Reconstructions shown in the upper row were obtained from data averaged over 10 slices (vertical resolution $500 \text{ }\mu\text{m}$), the corresponding reconstructions of a single slice of $50 \text{ }\mu\text{m}$ thickness are shown below.

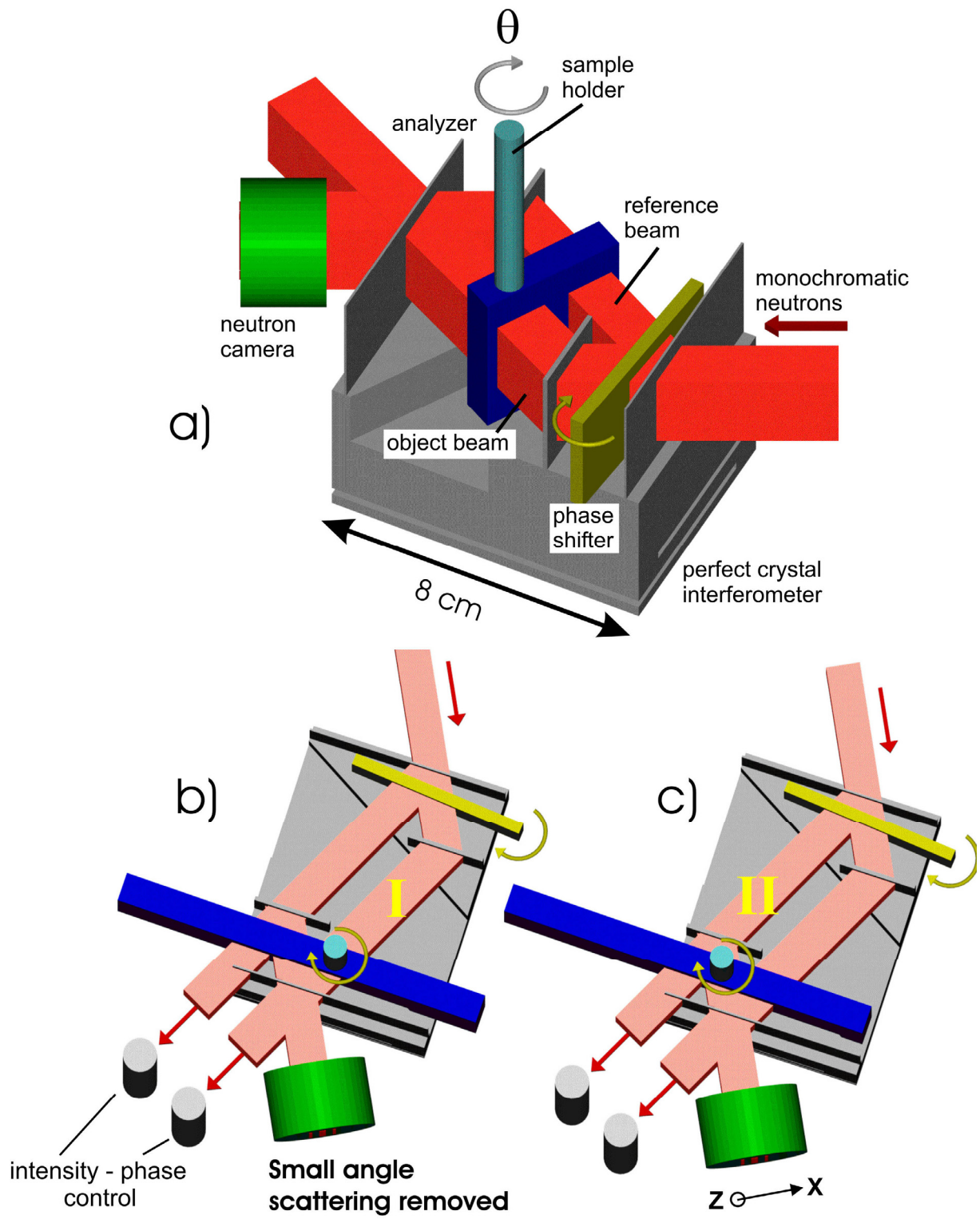


Fig. 1 – Zawisky

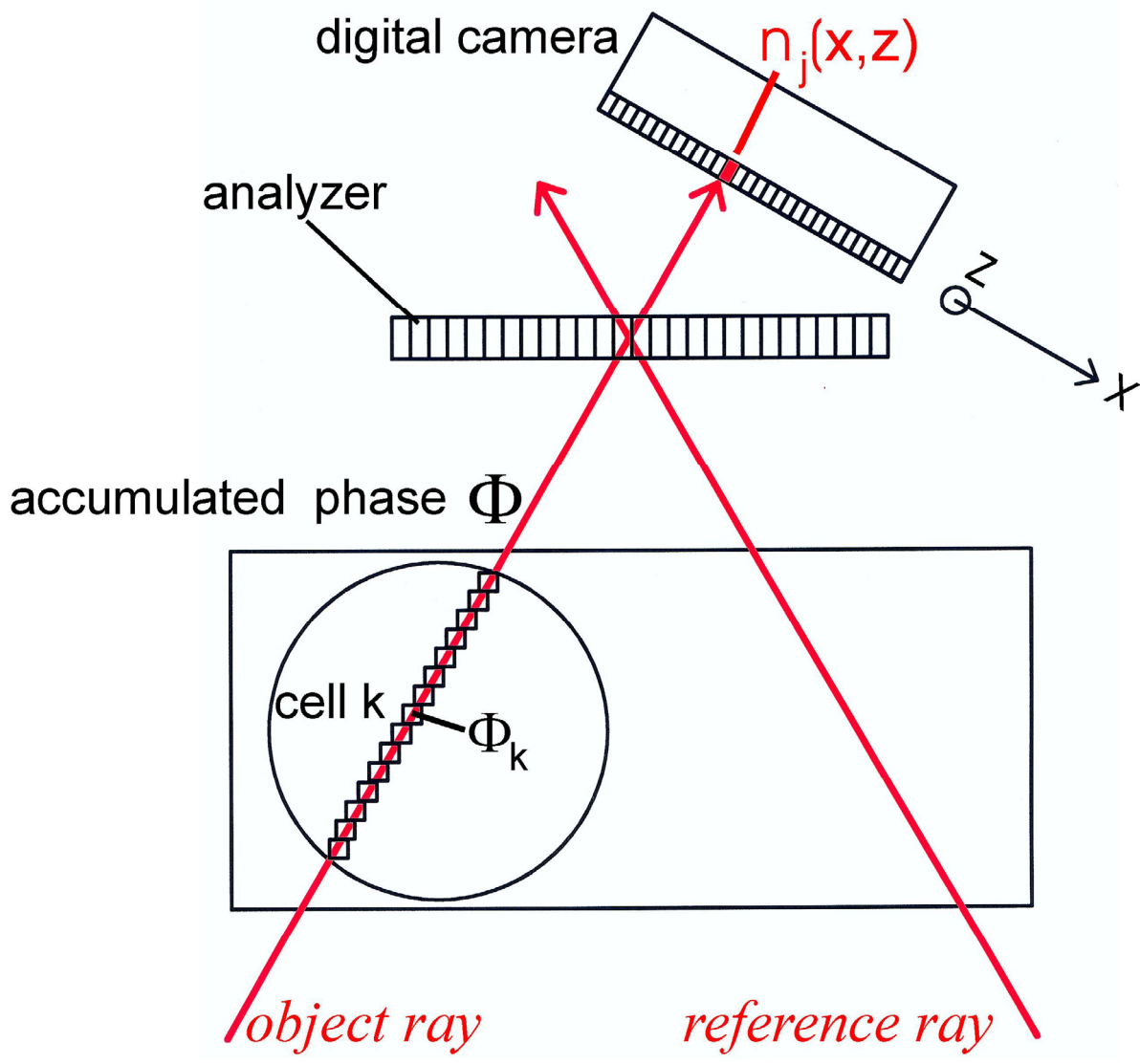


Fig. 2 - Zawisky

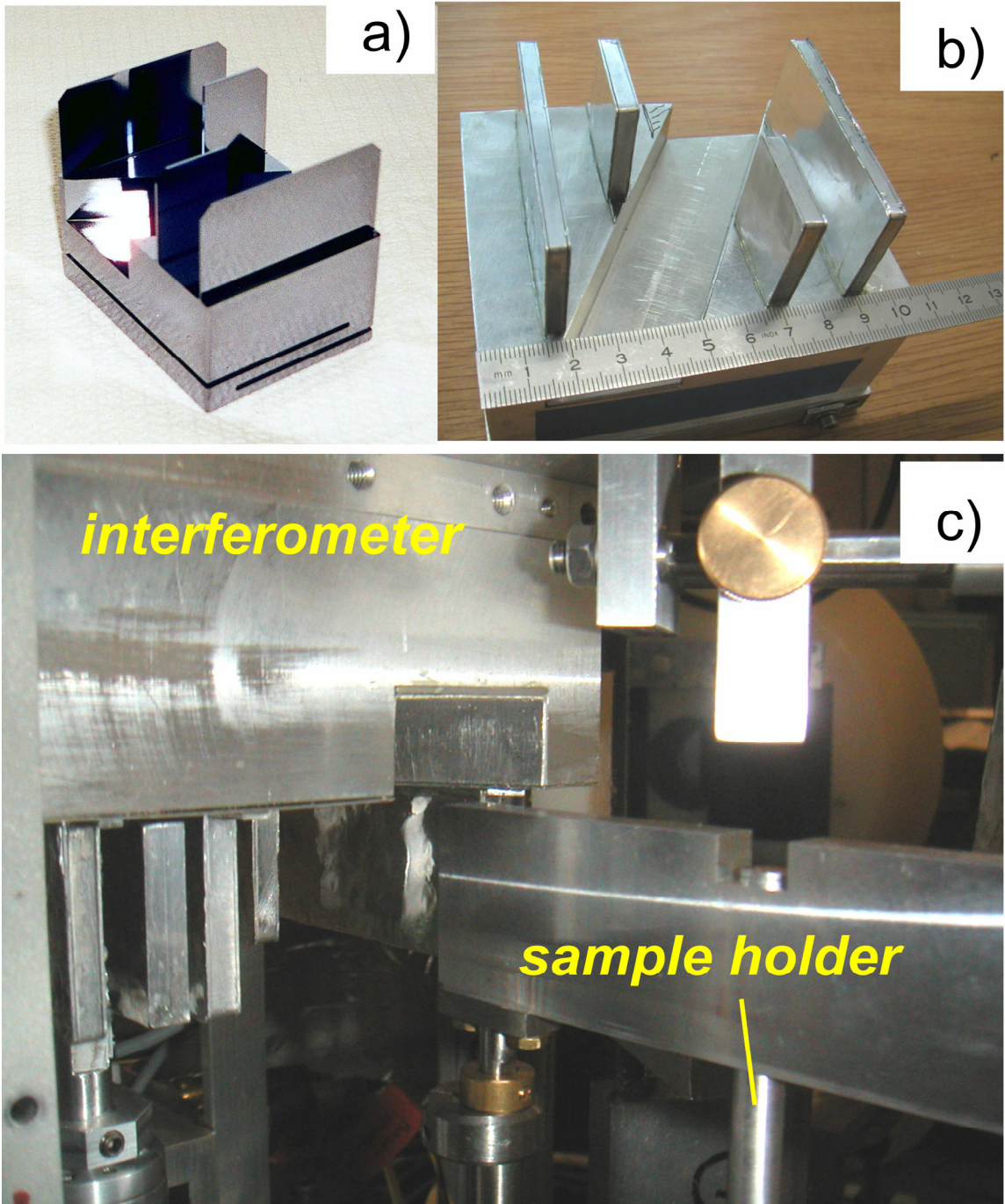


Fig. 3 - Zawisky

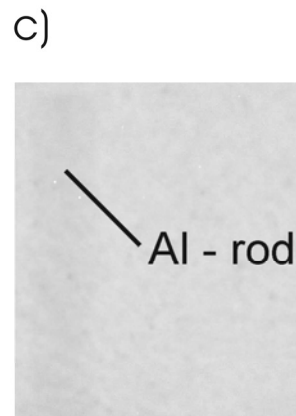
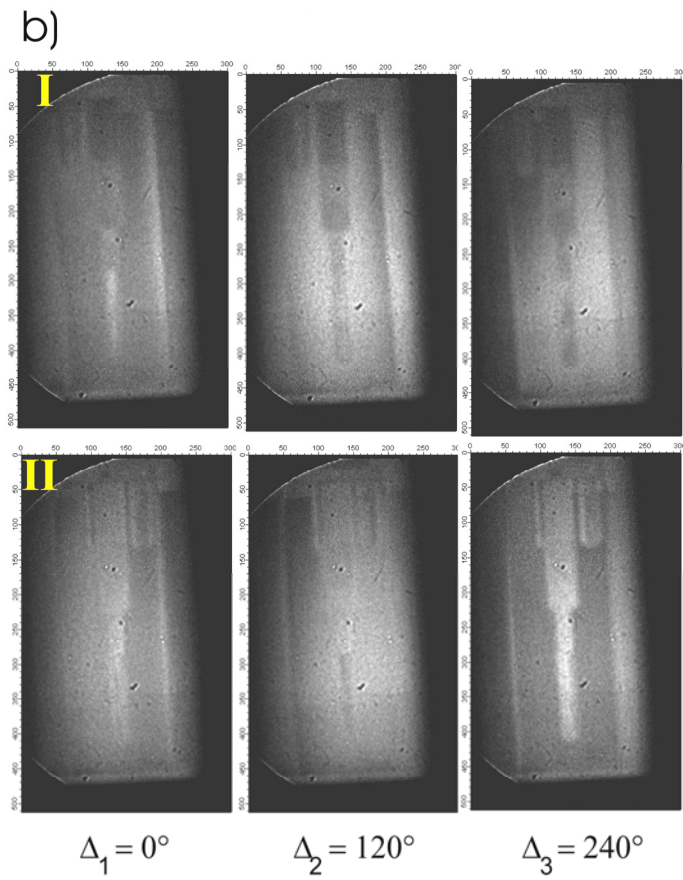
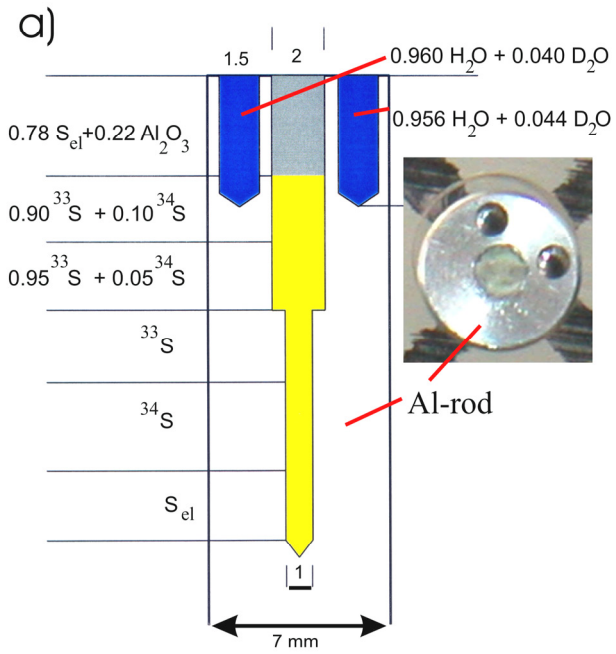


Fig. 4 - Zawisky

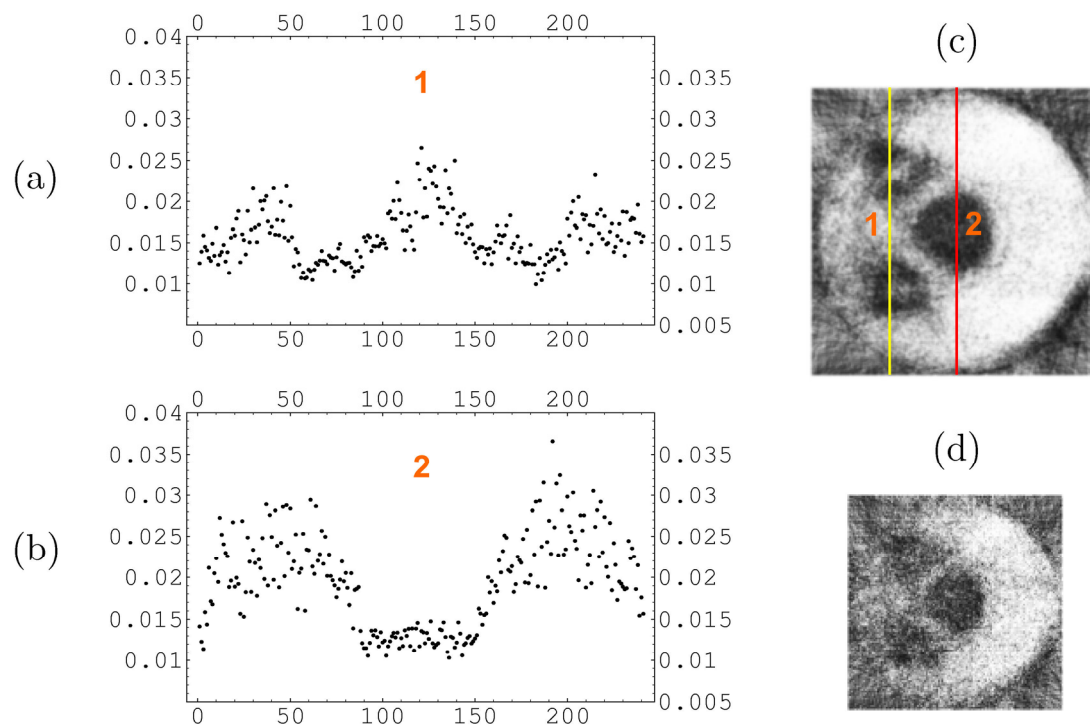
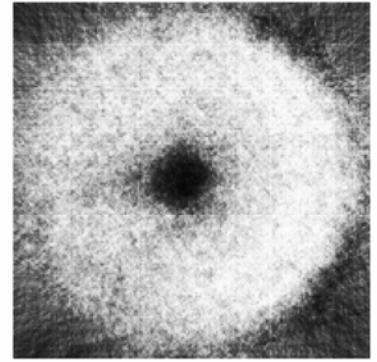
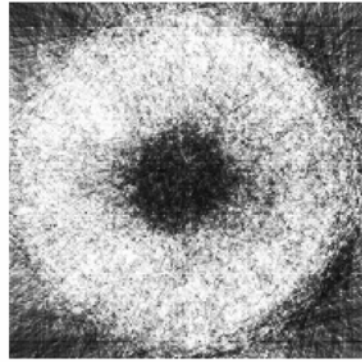
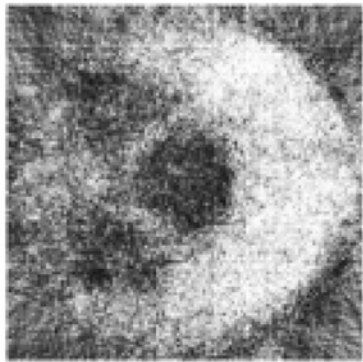
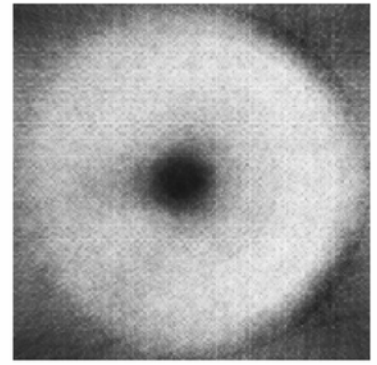
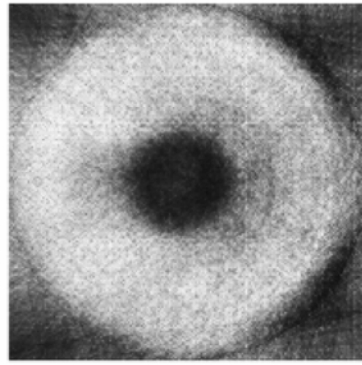
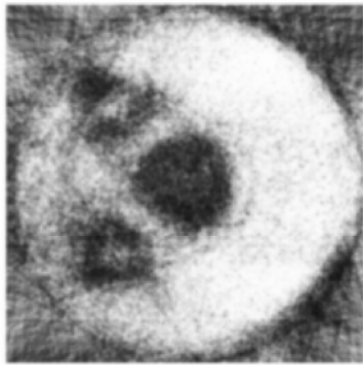


Fig. 5 – Zawisky



(a)

(b)

(c)

Fig. 6 - Zawisky